J. Fluid Mech. (2003), *vol.* 475, *pp.* 357–375.
DOI: 10.1017/S0022112002002896 Printed in the United Kingdom

Dynamics of target patterns in low-Prandtl-number convection

By JENNIFER H. SIGGERS†

Department of Applied Mathematics and Theoretical Physics, Centre for Mathematical Sciences
University of Cambridge, Wilberforce Road, Cambridge CB3 0WA, UK

(Received 20 September 2001 and in revised form 25 February 2002)

Axisymmetric Rayleigh–Bénard convection in a cylinder with vertical axis is studied. The nonlinear behaviour is investigated near the onset of convection using an eigenfunction expansion. It is found that initially a steady target pattern develops; the number of rolls depends only on the aspect ratio of the box. At about 5% beyond onset, an oscillatory pattern develops, in which the number of rolls oscillates between two adjacent values. The transitions between the initial steady state and this oscillatory pattern are also investigated, and fall into two main categories. As the Rayleigh number is reduced to the transition point, either the period of the travelling wave tends to infinity, whilst its amplitude stays finite, or there is a sudden transition to a vascillating pattern, the amplitude of which becomes smaller and finally vanishes, whilst the period remains finite. The results are compared with experimental work.

1. Introduction

Rayleigh–Bénard convection is known to exhibit a wealth of different patterns. In this paper, axisymmetric convection in a cylinder is considered, and the transition from steady patterns of concentric rings, called targets, to a pattern of travelling waves is investigated. Many convection experiments have produced target patterns, for example those by Koschmieder (1993) and Plapp, Egolf & Bodenschatz (1998). Such patterns form most readily in low- or moderate-Prandtl-number fluids and in large aspect ratio systems. However, relatively little is understood about their dynamics. This paper is an investigation into the dynamics of axisymmetric patterns and examines the formation of an axisymmetric radially travelling wave. As well as in convection, target patterns form in many other systems, for example the Belousov–Zhabotinsky reaction (Vidal *et al.* 1986) and other reaction–diffusion experiments, slime mould (Weijer 1999), catalysis experiments (Berdau *et al.* 1997), and Faraday experiments (Edwards & Fauve 1994), and so the results in this paper may shed light on these other systems.

The axisymmetric Rayleigh–Bénard convection equations are investigated in a fluid-filled cylindrical box with vertical axis. Tuckerman & Barkley (1988) also studied this system using a Prandtl number of 10 and an aspect ratio of 5: they found a travelling wave in which the concentric rings in travel inwards. Here, the analysis of that paper is extended to include a continuously varying aspect ratio in the approximate range $4 \leqslant \Gamma \leqslant 10$, and the Prandtl number takes the fixed value 0.1. A detailed bifurcation study is performed and a similar oscillatory pattern is also found for all aspect

† Present address: School of Mathematical Sciences, University of Nottingham, University Park, Nottingham NG7 2RD, UK.

ratios for Rayleigh numbers above about 5% beyond onset, but it is formed by a different mechanism and the rolls in the travelling wave travel *outwards* rather than inwards. The mechanism of its formation involves one or more global bifurcations; their precise nature depends on the aspect ratio. Hu, Ecke & Ahlers (1993) also found a similar periodic orbit experimentally, using Prandtl number 0.93 and aspect ratio 41. Behringer & Gao (1983) investigated the onset of time-dependence in convection in a cylinder, finding a travelling wave far above onset. The transition could occur in two qualitatively different ways, depending on the aspect ratio. In one the period of the travelling wave tends to infinity whilst the amplitude stays finite and in the other, the amplitude tends to zero while the period stays non-zero.

In § 2, the eigenfunctions of the Rayleigh–Bénard convection equations are derived and equations describing the evolution of the amplitudes of these eigenfunctions are found. In § 3, the solutions of these equations are investigated for a fixed value of the Prandtl number. All the solutions and their stability are found close to onset for aspect ratios between 6.68 and 8.10. Finally, in § 4, these results and their applications are discussed.

2. Derivation of amplitude equations

In this section the Rayleigh–Bénard convection equations and the boundary conditions to be used are described. The eigenfunctions of the linearized system are calculated and the marginal stability curves are plotted in parameter space. Finally the evolution equations for the amplitudes of the eigenfunctions are derived and the choice of truncation is discussed.

2.1. *Rayleigh–Bénard equations*

The Boussinesq approximation is used and the variables are rescaled to simplify the equations to their standard form:

$$\frac{\partial \boldsymbol{u}}{\partial t} + (\boldsymbol{u}\cdot\nabla)\boldsymbol{u} = -\nabla p + \sigma R\theta\hat{\boldsymbol{z}} + \sigma\nabla^2\boldsymbol{u}, \tag{2.1a}$$

$$\frac{\partial \theta}{\partial t} + (\boldsymbol{u}\cdot\nabla)\theta = \nabla^2\theta + \boldsymbol{u}\cdot\hat{\boldsymbol{z}}, \tag{2.1b}$$

$$\nabla\cdot\boldsymbol{u} = 0, \tag{2.1c}$$

to be solved in a cylindrical box of height one and radius Γ. In (2.1) $\hat{\boldsymbol{z}}$ is a unit vector in the vertical direction, $\boldsymbol{u}$ is the scaled velocity of the fluid, and θ is related to the fluid temperature T by $T = T_0 + (1 - z + \theta)\Delta_T$. The Prandtl number σ is ν/κ_T and the Rayleigh number R is given by $d^3 g\alpha_T\Delta_T/\kappa_T\nu$, where κ_T is the thermal diffusivity, ν is the kinematic viscosity, g is the acceleration due to gravity, d is the depth of the layer, α_T is the thermal expansion coefficient and Δ_T is the temperature difference across the layer.

Stress-free, rather than non-slip, boundary conditions are used in order to simplify the analysis, together with insulating sidewall boundary conditions. In the cylindrical container these are

$$u_r = \frac{\partial}{\partial r}\left(\frac{u_\phi}{r}\right) = \frac{\partial u_z}{\partial r} = \frac{\partial \theta}{\partial r} = 0 \quad \text{at} \quad r = \Gamma, \tag{2.2a}$$

$$\frac{\partial u_r}{\partial z} = \frac{\partial u_\phi}{\partial z} = u_z = \theta = 0 \quad \text{at} \quad z = 0, 1. \tag{2.2b}$$

With these boundary conditions, the linearization of the system (2.1) is self-adjoint and so the eigenvalues are all real, and the eigenfunctions are pairwise orthogonal.

In order to investigate the possible solutions of these equations an eigenfunction expansion is used. The system (2.1) is linearized and solved to give the eigenfunctions. The variables $(\boldsymbol{u}, \theta)$ are written as a sum of the eigenfunctions, each multiplied by an amplitude. These expressions are substituted into the full nonlinear equations (2.1), yielding a set of ordinary differential equations whose solutions approximate those of the full system (2.1). If enough eigenfunctions are used in the truncation, then this method essentially solves (2.1) using a spectral method. However, here the aim is to use a more manageable number of equations so that the details of the solution can be found for a continuous range of parameter values rather than at isolated points as would be the case for a full simulation.

2.2. *Solution of the linearized equations*

In this section the equations (2.1) are linearized and their axisymmetric eigenfunctions found. In a cylindrical container the eigenfunctions involve Bessel functions in the radial direction (Liang, Vidal & Acrivos 1969; Jones, Moore & Weiss 1976). The method used here is based on ideas from Rosenblat, Davis & Homsy (1982) and similar work was also done by Charlson & Sani (1970). Batchelor & Nitsche (1993) also found the eigenfunctions in an infinite vertical cylinder and their work agrees with that presented here. This is a consequence of the relationship between periodic and Neumann boundary conditions for elliptic operators (see e.g. Crawford *et al.* 1991). The eigenfunctions fall into two categories: those without vertical vorticity, called poloidal modes, and those with non-zero vertical vorticity, called toroidal. The toroidal eigenfunctions have only $SO(2)$ symmetry, whereas the poloidal eigenfunctions have $O(2)$ symmetry. However, the primary branches have $O(2)$ symmetry, meaning that the solutions on these branches are poloidal and the toroidal eigenfunctions may only contribute to a solution after a secondary bifurcation. However, it was found that such a bifurcation did not occur, and so for brevity the toroidal eigenfunctions are omitted.

The velocity and temperature fields are written as a sum of separable solutions of $\nabla^2\boldsymbol{u} = -\alpha^2\boldsymbol{u}$ and $\nabla^2\theta = -\alpha^2\theta$ in cylindrical polar coordinates (r, ϕ, z). Stress-free boundary conditions are used and splitting the velocity and temperature components simplifies the analysis and enables better comparison with previous work, for example the Lorenz equations (Lorenz 1963). The eigenfunctions at the zero solution are

$$\boldsymbol{u}_{kn} = \left(-\frac{n\pi}{\lambda_k} J_1(\lambda_k r)\cos(n\pi z), 0, J_0(\lambda_k r)\sin(n\pi z)\right),$$

$$\theta_{kn} = J_0(\lambda_k r)\sin(n\pi z),$$

where J_m is the Bessel function of the first kind of order m; $k, n \in \mathbb{N}$, where $\lambda_k = j_{1k}/\Gamma$ and j_{1k} is the kth positive solution of $J_1(x) = 0$; α_{kn}^2 is given by $\lambda_k^2 + n^2\pi^2$. The linear growth rate s of the amplitude of the eigenfunction is a solution of

$$\alpha_{kn}^2(\alpha_{kn}^2 + s)(\alpha_{kn}^2 + s/\sigma) = R\lambda_k^2. \tag{2.3}$$

The eigenfunction $\boldsymbol{u}_{kn}$ has k rolls in the radial direction and n rolls in the vertical direction. The neutral stability curves are shown in figure 1. As the temperature difference across the layer increases from zero, the first non-trivial patterns would be seen as these curves are crossed – these are steady targets; the number of rolls in the target depends on the value of k in the corresponding eigenfunction $(\boldsymbol{u}_{k1}, \theta_{k1})$.

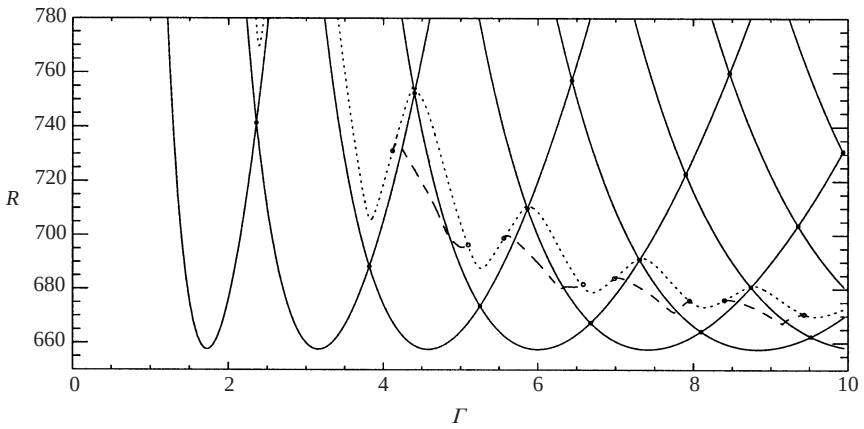

FIGURE 1. The marginal stability curves (solid curves) of the eigenfunctions $(\boldsymbol{u}_{k1}, \theta_{k1})$ for various values of k. The curves for $(\boldsymbol{u}_{kn}, \theta_{kn})$ for larger n lie at much higher Rayleigh numbers. The solid circles mark the points of intersection of these curves, which are codimension-two points. Also plotted are the saddle-node bifurcations (dotted curves), Hopf bifurcations (dashed curves) and Takens–Bogdanov points (open circles). These will be explained later, and are found using the set of modes $S = \{(k,1) : 1 \leqslant k \leqslant 7, (k,2) : 1 \leqslant k \leqslant 14\}$ for $\Gamma < 3.9$ for the saddle-nodes and for $\Gamma < 6.7$ for the Hopf bifurcations and for larger Γ, $S = \{(k,1) : 1 \leqslant k \leqslant 10, (k,2) : 1 \leqslant k \leqslant 20\}$.

With non-slip boundary conditions, the eigenfunctions would be a linear superposition of three different Bessel functions, depending on all three parameters R, Γ and σ, and would need to be recalculated every time the parameters change, a process involving finding the roots of a cubic equation that would take a substantial amount of time. In the stress-free case, the only parameter dependence is on Γ.

Having found the eigenfunctions, the system of partial differential equations (2.1) may be converted into a set of ordinary differential equations by truncation.

2.3. *Time evolution equations for the amplitudes of the eigenfunctions*

In order to investigate the system (2.1) a finite set of the eigenfunctions is chosen. The amplitude of all the other eigenfunctions is assumed to be zero. Let $S = \{(k_i, n_i) : i = 1, 2, \ldots q\}$, represent the finite set of eigenfunctions $\{\boldsymbol{u}_i, \theta_i : 1 \leqslant i \leqslant q\}$ to be used, where $\boldsymbol{u}_i$ is an abbreviation for $\boldsymbol{u}_{k_i,n_i}$ etc. Thus the velocity and temperature fields are approximated by $\boldsymbol{u} = \sum_{i\in S} a_i \boldsymbol{u}_i$, $\theta = \sum_{i\in S} b_i \theta_i$. Substiting these expressions into the governing equations (2.1) gives equations describing the evolution of the amplitudes:

$$\dot{a}_i = \frac{\sigma R \lambda_i^2}{\alpha_i^2} b_i - \sigma \alpha_i^2 a_i + \sum_{j,k\in S} a_j a_k \frac{\langle \boldsymbol{u}_i \cdot (\boldsymbol{u}_j \times \boldsymbol{\omega}_k)\rangle}{\langle |u_i|^2 \rangle} \tag{2.4a}$$

$$\dot{b}_i = a_i - \alpha_i^2 b_i - \sum_{j,k\in S} a_j b_k \frac{\langle \theta_i \boldsymbol{u}_j \cdot \nabla \theta_k \rangle}{\langle |\theta_i|^2 \rangle}. \tag{2.4b}$$

If a_i is mapped to $(-1)^{n_i} a_i$ and b_i to $(-1)^{n_i} b_i$, then the equations are unchanged. This symmetry corresponds to reflecting the box in the horizontal midplane and its action will be denoted by κ.

S must contain sufficiently many elements to describe the dynamics accurately, but on the other hand the number of equations is $2q$ and the time taken for the computations increases dramatically with q. Thus it is important to choose S with care.

2.4. *Weakly nonlinear behaviour*

The method will only produce accurate results if the eigenfunctions omitted from S have very small amplitudes in the true solution. In order to decide which of the eigenfunctions may be neglected whilst still retaining an accurate solution, the weakly nonlinear behaviour of the equations is derived.

Parameter values such that the largest linear growth rate of any eigenfunction is small and positive are considered. These are points lying just above a neutral stability curve in figure 1, but not above any of the others. The values of σ and Γ are fixed and

$$R = R_0 + \epsilon R_1 + \epsilon^2 R_2 + \cdots,$$

$$\boldsymbol{u} = \epsilon \boldsymbol{u}_1 + \epsilon^2 \boldsymbol{u}_2 + \cdots,$$

$$\theta = \epsilon \theta_1 + \epsilon^2 \theta_2 + \cdots,$$

where

$$R_0 = \frac{((j_{1k_0}/\Gamma)^2 + \pi^2)^3}{(j_{1k_0}/\Gamma)^2}$$

is the value of R on the neutral stability curve corresponding to $(\boldsymbol{u}_{k_0 1}, \theta_{k_0 1})$ and ϵ is a small parameter. Then $\boldsymbol{u}_i$ and θ_i are expanded as

$$\boldsymbol{u}_i = \sum_{k,n} a^i_{kn} \boldsymbol{u}_{kn}, \qquad \theta_i = \sum_{k,n} b^i_{kn} \theta_{kn}.$$

These expressions are substituted into the governing equations. At each order in ϵ the resulting equations are multiplied by each eigenfunction in turn and integrated over the interior of the cylinder. To first order in ϵ

$$\boldsymbol{u}_1 = \alpha^2_{k_0 1} \boldsymbol{u}_{k_0 1}, \qquad \theta_1 = \theta_{k_0 1},$$

and $R_1 = 0$. At second order in ϵ, the only coefficients a^2_{kn} and b^2_{kn} that are non-zero are

$$a^2_{k2} = -\left(\frac{\alpha^2_{k2} \langle \boldsymbol{u}_{k2} \cdot (\boldsymbol{u}_1 \cdot \nabla \boldsymbol{u}_1) \rangle / \langle |\boldsymbol{u}_{k2}|^2 \rangle + (\sigma R_0 \lambda^2_k / \alpha^2_{k2}) \langle \theta_{k2} \boldsymbol{u}_1 \cdot \nabla \theta_1 \rangle / \langle \theta^2_{k2} \rangle}{(\sigma \lambda^2_k / \alpha^2_{k2})(\alpha^6_{k2}/\lambda^2_k - R_0)} \right),$$

$$b^2_{k2} = -\left(\frac{(\langle \boldsymbol{u}_{k2} \cdot (\boldsymbol{u}_1 \cdot \nabla \boldsymbol{u}_1) \rangle / \langle |\boldsymbol{u}_{k2}|^2 \rangle) + \sigma \alpha^2_{k2} \langle \theta_{k2} \boldsymbol{u}_1 \cdot \nabla \theta_1 \rangle / \langle \theta^2_{k2} \rangle}{(\sigma \lambda^2_k / \alpha^2_{k2})(\alpha^6_{k2}/\lambda^2_k - R_0)} \right).$$

Also,

$$R_2 = \frac{-\langle \boldsymbol{u}_1 \cdot \boldsymbol{u}_2 \times \boldsymbol{\omega}_1 \rangle + \sigma R_0 \langle \theta_1 \boldsymbol{u}_1 \cdot \nabla \theta_2 \rangle}{\sigma \langle w_1 \theta_1 \rangle},$$

$$= \sum_{k,n} \frac{1}{\sigma \langle w_1 \theta_1 \rangle} (-a^2_{kn} \langle \boldsymbol{u}_1 \cdot \boldsymbol{u}_{kn} \times \boldsymbol{\omega}_1 \rangle + b^2_{kn} \sigma R_0 \langle \theta_1 \boldsymbol{u}_1 \cdot \nabla \theta_{kn} \rangle),$$

where $\boldsymbol{\omega}_1 = \nabla \times \boldsymbol{u}_1$.

In order to compare how much effect the presence of each eigenfunction has at second order, the contributions to R_2 from the eigenfunction $\boldsymbol{u}_{k2}$ and θ_{k2} are calculated. Those eigenfunctions making very large contributions should certainly be included in the truncation. An example with $k_0 = 5$ is shown in figure 2. For this graph, Γ is

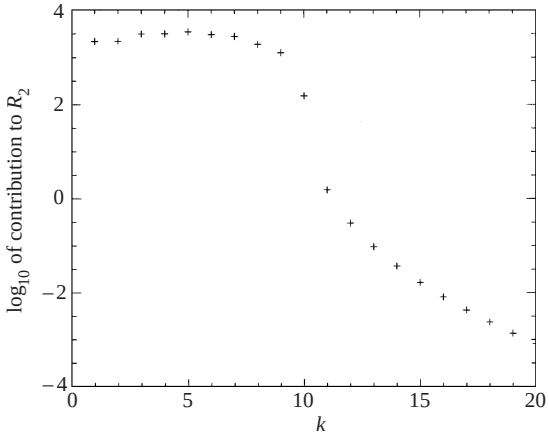

FIGURE 2. Contributions of the eigenfunction $(\boldsymbol{u}_{k2}, \theta_{k2})$ to R_2 for various values of k. Here, $k_0 = 5$ and the parameters are $\Gamma \approx 7.41$, $R_0 \approx 657.5$ and $\sigma = 0.1$. R_2 is equal to the sum of all these contributions.

chosen so that R takes its minimum value along the marginal stability curve, although the features of the graph are unchanged for any value of Γ in the region where the marginal stability curve for $(\boldsymbol{u}_{5,1}, \theta_{5,1})$ is lower than all the other curves in figure 1. In particular, the contributions decrease by about two orders of magnitude when k increases past $2k_0$ and continue decreasing as k is increased further. This feature occurs for all $k_0 \leqslant 20$ and all Γ.

This analysis seems to suggest that for values of R just above the critical value, the eigenfunctions $(\boldsymbol{u}_{k2}, \theta_{k2})$ for $k \leqslant 2k_0$ must be included in the truncation and that the rest may be discarded. That is $S = \{(k_0, 1), (k, 2) : 1 \leqslant k \leqslant 2k_0\}$. If the parameters (Γ, R) lie near the crossing point of two of the curves in figure 1, then the set of eigenfunctions needed is the union of the two sets for the cases where (Γ, R) just lies near one of the curves, that is $S = \{(k, 1) : k_0 \leqslant k \leqslant k_0 + 1, (k, 2) : 1 \leqslant k \leqslant 2k_0\}$.

However, it was found that this analysis does not predict a sufficient number of modes even to analyse modestly supercritical behaviour with R less than 10% above onset. In order to determine a suitable truncation, the set of modes used was gradually enlarged until no further qualitative changes in the behaviour were seen. It was found that $S = \{(k, 1) : k_0 \leqslant k \leqslant k_1, (k, 2) : 1 \leqslant k \leqslant 2k_1\}$ for some $k_1 > k_0$ was needed. The minimal value of $k_1 - k_0$ required tended to increase as Γ increases.

3. Results

Many experiments that have produced targets used low Prandtl numbers (about 1 or less) (e.g. Hu *et al.* 1993; Rüdiger & Feudel 2000). Here, σ is fixed at 0.1 and the solutions of the set of equations (2.4) near onset are found and discussed.

3.1. *Behaviour for* $\Gamma \leqslant 10$

A branch-following program, AUTO (Doedel *et al.* 1997), was used to follow solutions of the truncated system as the parameters are gradually changed. First just the Rayleigh number was varied. Two examples for different aspect ratios are shown in figure 3. In order to build up the picture of what happens in parameter space, the values of R and Γ at different types of bifurcation are found. Starting from the saddle-node bifurcation point (solid triangle) in figure 3(*b*), Γ was allowed to vary

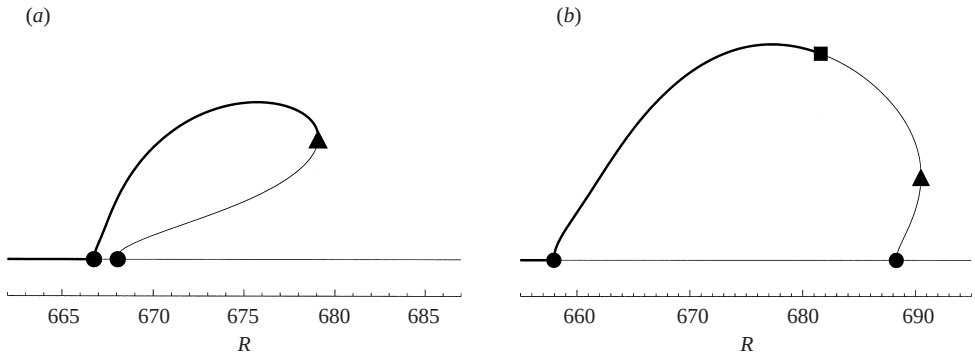

FIGURE 3. Bifurcation diagrams showing the steady solutions for (*a*) $\Gamma = 6.7$ and (*b*) $\Gamma = 7.25$. Stable solutions are shown by thick curves, solid circles represent pitchfork bifurcations, triangles represent saddle-node bifurcations and squares represent Hopf bifurcations. The truncation is given by $S = \{(k,1) : 4 \leqslant k \leqslant 8, (k,2) : 1 \leqslant k \leqslant 16\}$.

and the value of R at the saddle-node bifurcation point was computed. The resulting curve in the (Γ, R)–plane is shown in figure 1. In a similar way, the positions of the Hopf bifurcations were also found and are plotted on the same figure. These are always on the first primary branch of solutions. For all Γ the bifurcation diagram is qualitatively the same as either figure 3(*a*) or figure 3(*b*) depending on whether or not there is a Hopf bifurcation at that value of Γ. The diagram in figure 3(*a*) is qualitatively the same as that computed in Tuckerman & Barkley (1988), which was obtained from a numerical simulation of the axisymmetric equations using $\Gamma = 5$ and $\sigma = 10$ and non-slip boundary conditions.

The ranges for Γ whose endpoints are given by the lowest set of codimension-two points marked with solid circles in figure 1 are

$$(2.36, 3.82), (3.82, 5.25), (5.25, 6.68), (6.68, 8.10), (8.10, 9.52), \ldots .$$

In each of these ranges, the behaviour is similar. Since the full details of the transitions in behaviour are quite complex, for the next section Γ is restricted to just one of these ranges, (6.68, 8.10), for ease of computation. The behaviour is thought to be similar in the other regions.

For all values of $\Gamma \in (5, 10)$, if R was taken above the saddle-node curve then for almost all initial conditions, the solution tended towards a periodic orbit, An example of the behaviour on this orbit is given in figure 4, which shows the motion of the fluid on a cross-section through the cylinder. As can be seen, it is a pattern of outwardly travelling concentric rings. The number of rolls oscillates between 5 and 6. Such a travelling wave was found for all values of R and Γ lying above the curve of saddle-node bifurcations up to about $R = 700$. The orbit has a symmetry: starting from a given point in the orbit, upon advancing half a period around the orbit and applying κ, the original solution is again recovered. This spatio-temporal symmetry is denoted by $\tilde{\kappa}$. None of the bifurcations described so far can produce this periodic orbit. It cannot come from the Hopf bifurcation (dashed curve in figure 1), because that bifurcation initially produces small vascillations about the steady target solution. During these the rolls can move back and forth, but they cannot form a travelling wave since the oscillations only have a small amplitude. The mechanisms that give rise to this wave are investigated in § 3.2.

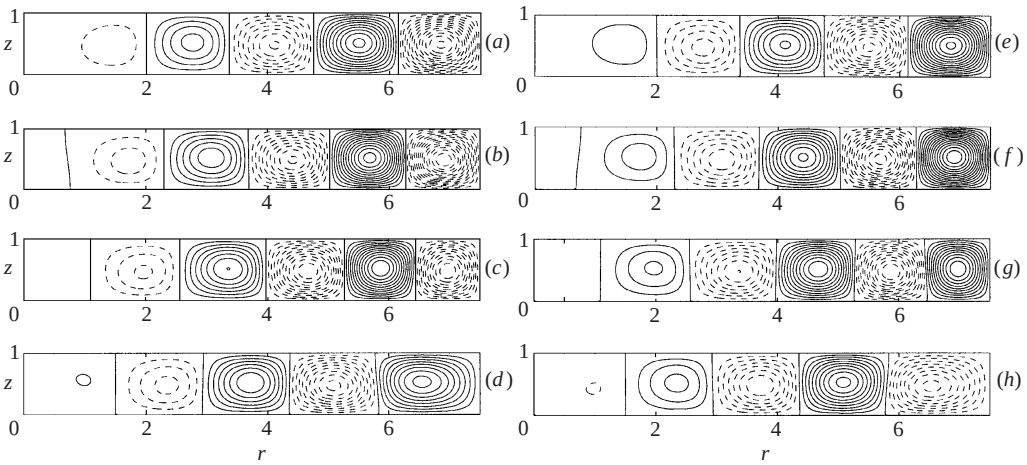

FIGURE 4. Streamlines of the travelling wave with $\Gamma = 7.5$ and $R = 690$, computed using $S = \{(k,1) : 4 \leqslant k \leqslant 8, (k,2) : 1 \leqslant k \leqslant 16\}$. The diagrams show snapshots of the solution at equally spaced intervals (one eighth of the period) on the periodic orbit. Solid curves indicate anti-clockwise motion and dashed curves indicate clockwise motion. The symmetry $\tilde{\kappa}$ is also evident: two diagrams that are half a period apart (e.g. (a) and (e)) are reflections of one another in the horizontal mid-plane (note that clockwise motion becomes anti-clockwise motion and vice versa under this transformation).

3.2. *Detailed behaviour for* $\Gamma \in (6.68, 8.10)$

The choice $S = \{(k,1) : 4 \leqslant k \leqslant 8, (k,2) : 1 \leqslant k \leqslant 16\}$ was found to be sufficient to describe qualitatively accurately all the steady state and Hopf bifurcations for $\Gamma \in (6.68, 8.10)$. Thus this choice of S is used and is assumed to be sufficient to describe all the behaviour near onset in this region. AUTO is used to follow the various curves in parameter space and figure 5(a) gives the complete picture of all the bifurcations in this range of Γ. The bifurcation diagrams for certain fixed values of Γ marked on figure 5(a) are given in figure 6. A brief description of the transitions in behaviour in each diagram follows.

(i) Figure 6(a) $(6.6 < \Gamma < 6.94)$. As R is increased past the initial pitchfork bifurcation, a stable branch of five roll target solutions is created, similar to that shown in figure 7(i), and the trivial solution becomes unstable. Just after the bifurcation, the solution is almost the pure eigenfunction $\boldsymbol{u}_{51}$, but as R increases, other modes with different numbers of rolls contribute significantly to the solution, although the overall pattern still has five rolls, figure 7(ii). At the second pitchfork bifurcation at $R = 671.1$, a branch of four roll solutions, similar to figure 7(iv) is created. These solutions are unstable and so would not be seen in an experiment. The solutions on this second branch soon develop a fifth roll, figure 7(iii). As R is increased, the two branches become closer together, meeting and annihilating at the saddle-node bifurcation.

There is also a global bifurcation, giving rise to a periodic orbit with symmetry $\tilde{\kappa}$. The periodic orbit is stable if and only if $\delta > 1$ where $\delta = -\lambda_-/\lambda_+ > 0$ and λ_+ is the positive eigenvalue at the saddle-point and λ_- is the largest negative eigenvalue there (see Guckenheimer & Holmes 1986). Figure 5(b) shows a graph of the values of δ as Γ varies. If the aspect ratio is less than 6.86 then $\delta > 1$ so the periodic orbit is stable, but for aspect ratios greater than 6.86 it is unstable when it is formed, but soon undergoes a saddle-node bifurcation to become stable. The global

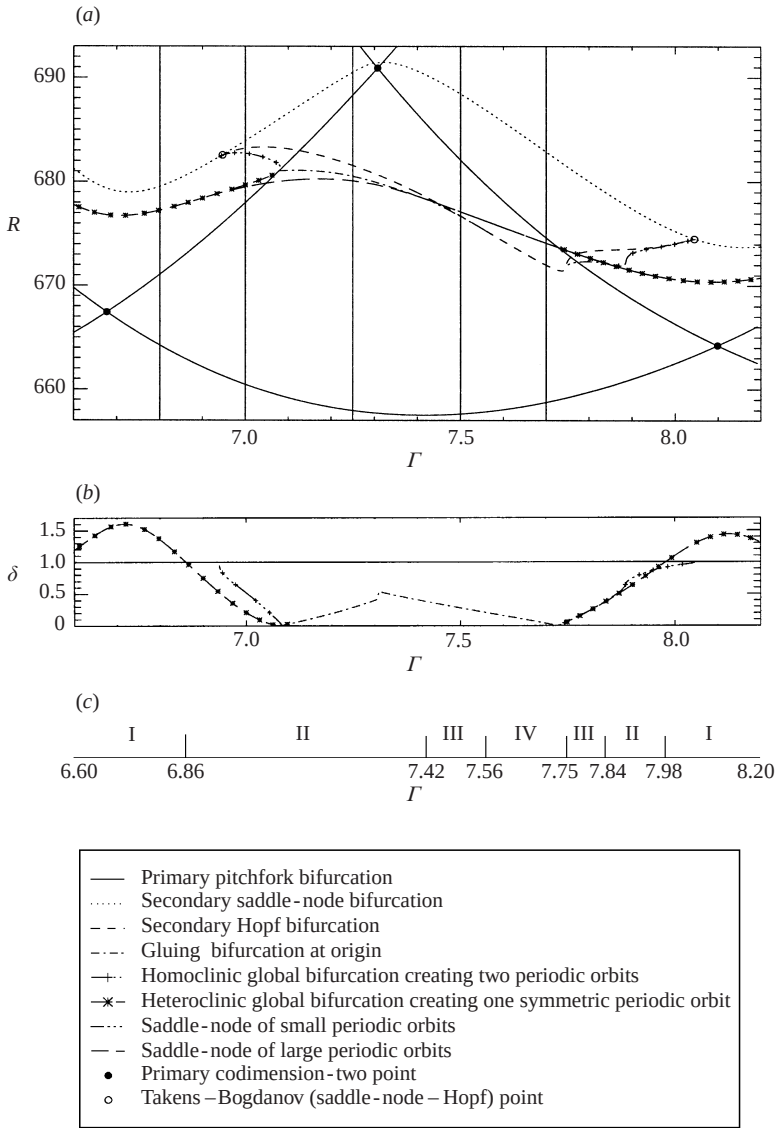

FIGURE 5. (*a*) The two-parameter unfolding to show the curves of saddle-node, Hopf and global bifurcations. The vertical lines show the constant-Γ cuts on which the bifurcation diagrams will be drawn. (*b*) Graphs of the eigenvalue ratio δ at the global bifurcations. (*c*) The ranges of Γ in which the transitions between stable solutions are qualitatively the same – there are four qualitatively different types of behaviour, labelled I, II, III and IV. These will be discussed at the end of this section.

bifurcation occurs in an attracting two-dimensional submanifold of the space spanned by all the amplitudes a_i and b_i. Schematic diagrams showing the dynamics on this manifold at the global bifurcation for $\Gamma < 6.86$ are given in figure 8(*a*)–(*c*). Before the bifurcation, 8(*a*), for almost all initial conditions, the solution tends to a steady pattern of concentric rings. At the bifurcation point, 8(*b*), a stable heteroclinic orbit is formed, meaning that afterwards, 8(*c*), the solution may either tend to a pattern of concentric rings or to the periodic orbit, depending on the initial conditions.

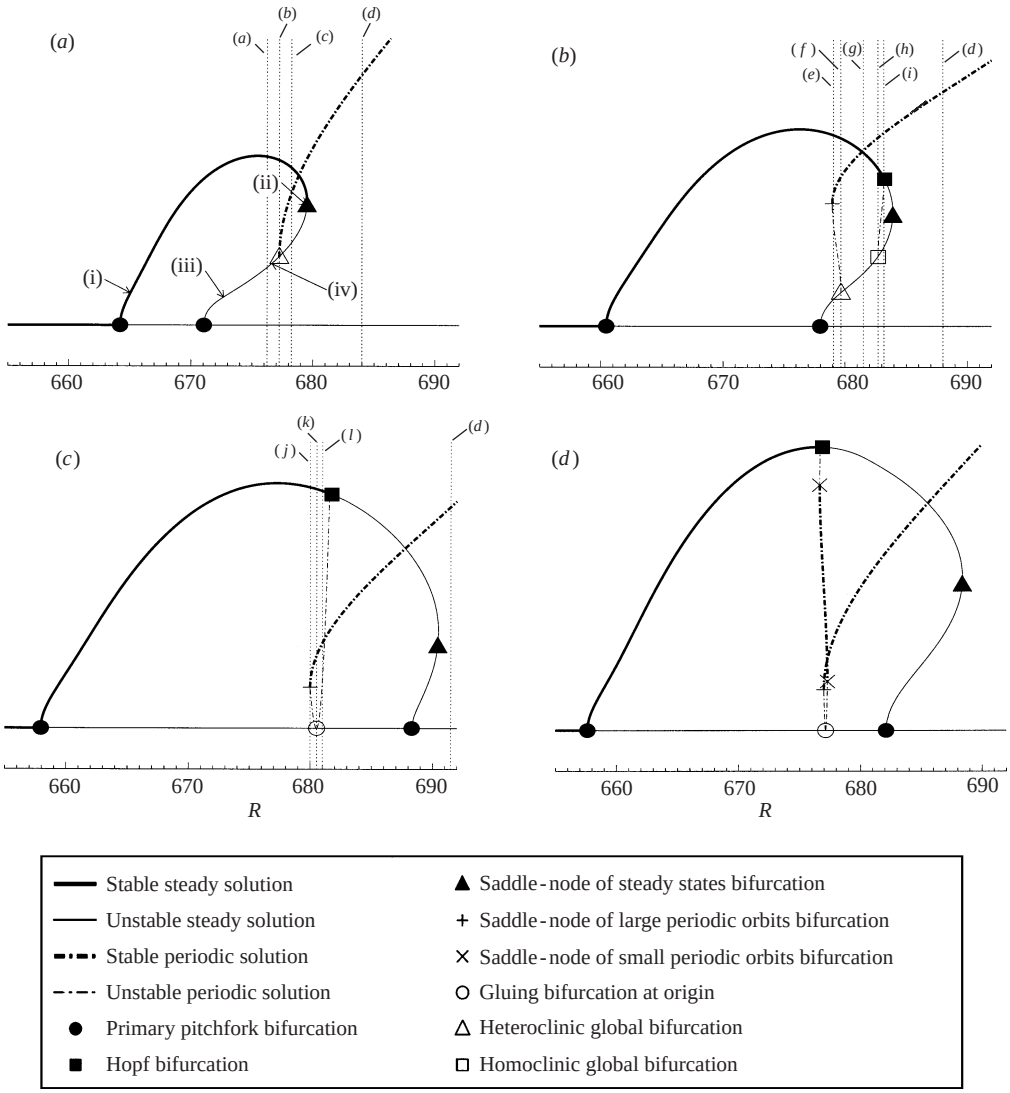

FIGURE 6. Bifurcation diagrams on the constant-Γ cuts shown in figure 5(a). The vertical axis shows the amplitude of the solution, which is the square root of $\sum_i (a_i^2 + b_i^2)$ for steady solutions, but is only qualitative for periodic solutions. (a) $\Gamma = 6.8$, (b) $\Gamma = 7.0$, (c) $\Gamma = 7.25$, (d) $\Gamma = 7.5$. The vertical dotted lines (a–l) correspond to the phase portraits drawn in figure 8.

For $\Gamma > 6.86$ the corresponding phase portraits are shown in figures 8(e), 8(f) and 8(g). At the saddle-node bifurcation all steady solutions except the trivial one are annihilated, and the phase portrait is shown in 8(d), consisting of the stable travelling wave and the unstable trivial solution. All non-zero initial conditions lead to the travelling wave, and this scenario occurred for all aspect ratios for larger Rayleigh numbers.

(ii) Figure 6(b) ($6.94 < \Gamma < 7.08$). As Γ increases beyond 6.94, the Takens–Bogdanov point (see Guckenheimer & Holmes 1986) is passed, see figure 9(a), giving rise to a Hopf bifurcation, on the first branch and a global bifurcation on the second branch. The transitions at the global bifurcation are shown in figures 8(g), 8(h) and

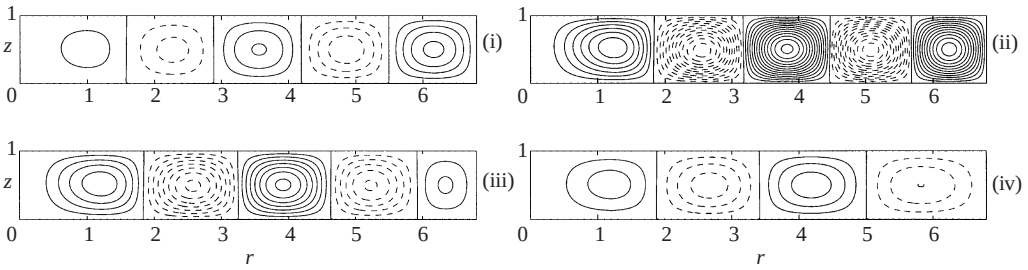

FIGURE 7. Streamlines of the steady solution on a cross-section of the cylindrical box at the corresponding labelled points in the bifurcations diagram figure 6(*a*). The values of R are: (i) $R \approx 665.0$, (ii) $R \approx 679.5$, (iii) $R \approx 676.6$, (iv) $R \approx 672.7$. Solid curves indicate anti-clockwise rotation and dashed curves indicate clockwise rotation.

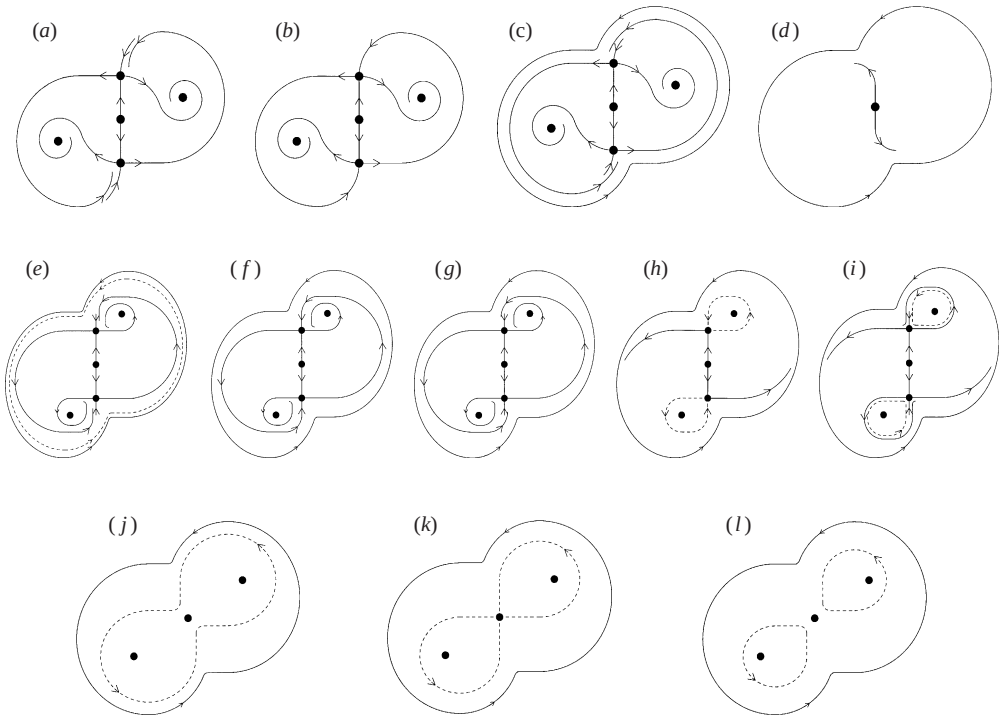

FIGURE 8. Qualitative phase portraits on the attracting two-dimensional manifold of the system at for various parameter values shown by vertical dotted lines in figure 6. The axes are amplitudes of two of the modes, for example a_1 and a_2. Steady solutions are shown by solid circles and the curves show some representative trajectories. (*a*), (*b*) and (*c*) The creation of a stable periodic orbit in a heteroclinic global bifurcation. (*d*) The state of the system at large Rayleigh numbers for all aspect ratios. (*e*), (*f*) and (*g*) The destruction of an unstable periodic orbit in the heteroclinic bifurcation and (*g*), (*h*) and (*i*) The creation of two unstable periodic orbits in a homoclinic bifurcation. (*j*), (*k*) and (*l*) The gluing bifurcation. In these diagrams, κ acts as a rotation through 180° about the origin.

8(*i*). In this, two small periodic orbits are created that are reflections of each other in κ. Again, these orbits are stable if and only if $\delta > 1$, but in this case, $\delta < 1$ (see figure 5*b*) so they are unstable.

(iii) Figure 6(*c*) ($7.08 < \Gamma < 7.42$). As Γ increases past 7.08, the two curves of global bifurcations collide and form a single curve of global gluing bifurcations as

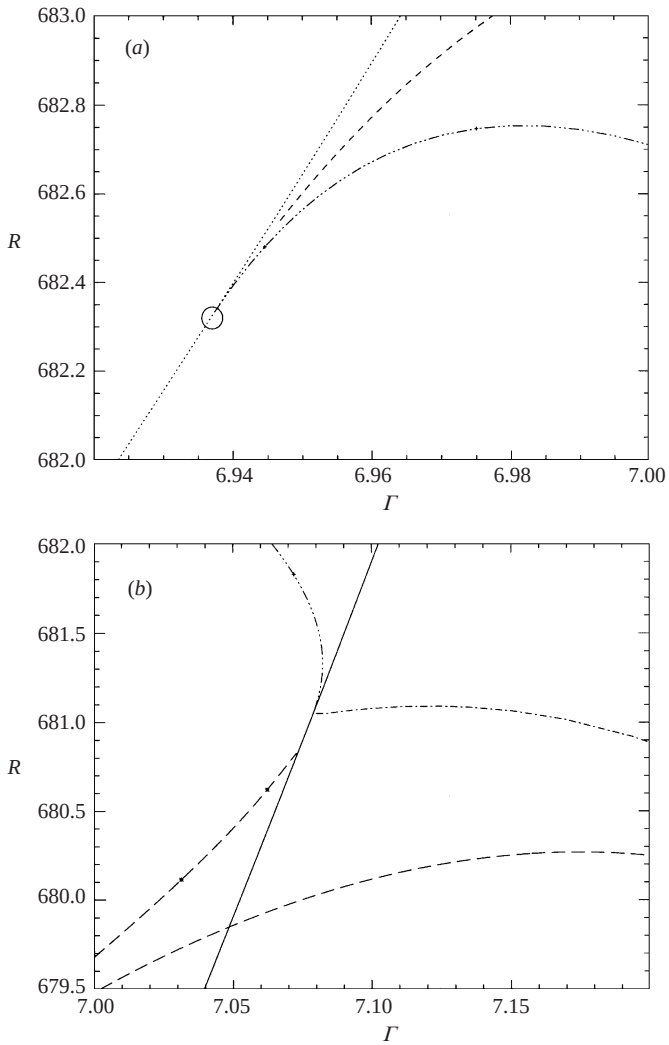

FIGURE 9. Enlargements of two regions of figure 5(*a*) showing (*a*) the Takens–Bogdanov point (indicated by an open circle), at which the curve of saddle-node bifurcations (dotted) absorbs a curve of Hopf bifurcations (dashed) and also a curve of global bifurcations (dash-dot-dot-dot), and (*b*) the two curves of global bifurcations (dash-dot-dot-dot and long dash curves) colliding at $\Gamma = 7.08$, $R = 681.0$ on the curve of pitchfork bifurcations (solid curve) and forming a single curve of gluing bifurcations (dot-dash curve). Also shown is the curve of saddle-node bifurcations (dashed), although this is not involved in the transitions.

they cross the curve of pitchfork bifurcations, see figure 9(*b*). The changes at the gluing bifurcation are in figures 8(*j*), 8(*k*) and 8(*l*), which shows how the periodic orbit collides with the origin, forming two smaller periodic orbits. The transitions from the heteroclinic–homoclinic bifurcation mechanism to the gluing bifurcation mechanism as the curve of pitchforks is crossed may be examined theoretically in a neighbourhood of parameter space, see the Appendix. All the gluing bifurcations for $\Gamma \in (7.08, 7.73)$ have $0 < \delta < 1$ (see figure 5*b*), meaning that the periodic orbits involved are unstable.

(iv) Figure 6(*d*) ($7.42 < \Gamma < 7.73$). The only difference between figures 6(*c*) and 6(*d*) is that there are now two more saddle-node bifurcations involving the pair of

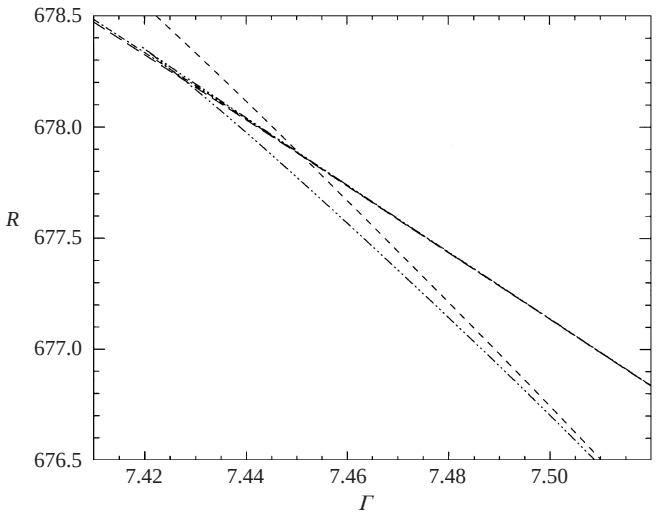

FIGURE 10. An enlargement of a region of figure 5(*a*) showing the cusp of saddle-node bifurcations (dash-dot-dot-dot curves). Towards the right-hand side of the picture the curve of saddle-nodes of periodic orbits with symmetry $\tilde{\kappa}$ (long-dashed) and the curve of gluing bifurcations (dash-dot) both become too close to the dash-dot-dot-dot curve to be distinguishable in this picture, the dash-dot-dot-dot curve remains above the dash-dot curve, which remains above the dotted curve.

small unglued periodic orbits, see figure 10. However, this will have an effect on the transitions between the stable solutions. As R is increased beyond the Hopf point a vascillating pattern of concentric rings would be seen, followed by the travelling wave. Both of these transitions occur in discontinuous jumps. At $\Gamma = 7.56$ the Hopf bifurcation becomes supercritical since one of the curves of saddle-node bifurcations that was created in the cusp is absorbed into the Hopf bifurcation and disappears. This means that the transition from steady convection to the vascillating pattern is now continuous.

For larger values of Γ on the right of figure 5(*a*), the sequence reverses except for the positions of the saddle-nodes of periodic orbits. Thus there is another pitchfork–gluing bifurcation at $\Gamma = 7.73$ and another cusp of saddle-node bifurcations at $\Gamma = 7.84$. At $\Gamma = 7.98$, the curve of saddle-nodes of large periodic orbits is absorbed into the curve of heteroclinic global bifurcations, so that the periodic orbit created in the bifurcation is now stable. Finally at $\Gamma = 8.05$ there is another Takens–Bogdanov bifurcation, so that for larger Γ, the bifurcation diagram is qualitatively the same as figure 6(*a*). The only difference at these larger aspect ratios is that the solution on the second primary branch now has six rolls rather than four, otherwise the transitions are qualitatively the same.

From this analysis, one may predict which stable patterns would be seen as the Rayleigh number and aspect ratio vary. In the following, C refers to the conduction state, S to a steady pattern of concentric rings, V to a vascillating pattern of rings and T to an outward travelling wave with symmetry $\tilde{\kappa}$. For any aspect ratio, C will be seen for low Rayleigh numbers, and at onset there is a smooth transition into S. Also, at high Rayleigh numbers (beyond about 5% above onset) T is always seen. For intermediate values of the Rayleigh number there are four qualitatively different scenarios:

I: as R is increased there is a discontinuous hysteretic transition from S to T, and on decreasing R the period of T tends to infinity before jumping discontinuously to S.

II: same as I, but the period of T does not become infinite as R is decreased.

III: as R is increased there is a discontinuous hysteretic transition from S to V and as R increases further there is another discontinuous hysteretic transition from V to T.

IV: same as III, but the transition from S to V is continuous and the amplitude of V tends to zero near this transition point (and the period remains finite).

Figure 5(c) shows the values of Γ where each of these types of behaviour occur. This agrees with the experimental results of Behringer & Gao (1983), in which Prandtl numbers in the range $0.54 < \sigma < 0.69$ were used. The aspect ratio was varied continuously in the range $4 < \Gamma < 13$. Behaviours I and IV were discovered.

4. Discussion

In this paper, the dynamics of axisymmetric convection has been completely described near onset for Prandtl number 0.1 for a range of aspect ratios. For all aspect ratios investigated, as the Rayleigh number increases beyond the critical point a steady target pattern develops in which the number of rolls depends only on the aspect ratio. On increasing the Rayleigh number further, this steady solution loses stability and a sequence of transitions takes place, ending with a travelling wave in which the concentric rings move radially outward. These secondary transitions take place at about 5% above onset for aspect ratios between 6.68 and 8.10, whilst for smaller aspect ratios they are further from onset and for larger ones they are closer to onset. The details of the secondary transitions vary with the aspect ratio, but there are two main mechanisms. The first has the travelling wave forming directly from the steady solution in a discontinuous hysteretic transition, whilst the second has an intermediate state in which the rolls merely vascillate but do not travel. Both of these scenarios were found in the experiments of Behringer & Gao (1983).

It may be thought that the work presented here might not relate well to experiments because of the use of unphysical stress-free boundary conditions. In fact, by the addition of some extra terms into the amplitude evolution equations (2.4), the neutral stability curves become qualitatively like those obtained with non-slip boundaries, that is they are continuous curves with no crossing points. Nonetheless, the bifurcation diagrams of steady state and Hopf bifurcations are qualitatively the same and the travelling wave was also present. So one can be fairly confident that, at least qualitatively, the results found will carry across to the case with non-slip boundaries.

As mentioned, Tuckerman & Barkley (1988) also obtained a similar travelling wave in a numerical investigation of axisymmetric Rayleigh–Bénard convection, using Prandtl number 10.0 and aspect ratio 5.0 together with non-slip velocity and conducting sidewall boundary conditions. The non-slip velocity conditions mean that the critical Rayleigh number is 1734. Their bifurcation diagram is shown in figure 11. The formation of the travelling wave is different. As the Rayleigh number is decreased through the saddle point, the period of the travelling wave becomes longer and finally infinite, giving the steady solution in a non-hysteretic continuous transition, which is different from the behaviour found in this paper. However, the mechanism is related to the heteroclinic global bifurcation mechanism since if the bifurcation (open triangle) in figure 6(a) moves up the branch until it coincides with the saddle-node bifurcation (solid triangle) then the bifurcation diagram in figure 11 will be obtained. Given that different parameters and boundary conditions were used, such a difference in the results is not surprising. Another difference is that the rolls in their travelling wave moved radially inward, whereas here they always travel outward, but this may be due to the different boundary conditions, Prandtl number or aspect ratio.

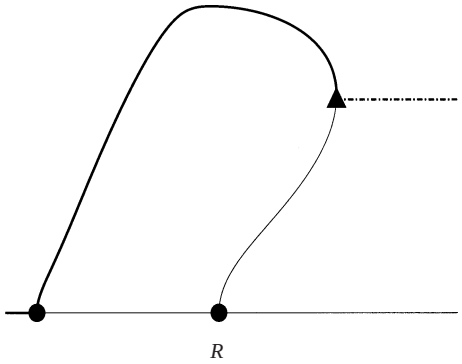

FIGURE 11. Bifurcation diagram obtained in Tuckerman & Barkley (1988), using non-slip boundary conditions, with $\sigma = 10.0$ and $\Gamma = 5.0$. The triangle marks the saddle-node bifurcation, which coincides with the global bifurcation in this case.

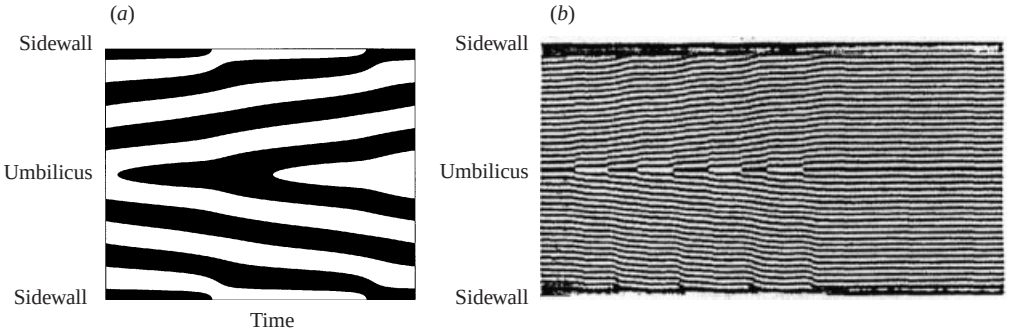

FIGURE 12. (*a*) The periodic orbit found for $\sigma = 0.1$, $\Gamma = 7.5$ and $R = 690$, which is about 5% above onset. (*b*) The periodic orbit found in Hu *et al.* (1993), reproduced with permission, for $\sigma = 0.93$, $\Gamma = 41$ and $R \approx 1875$, which is about 10% above onset. Black indicates upward moving fluid in the horizontal midplane and white indicates downward moving fluid there. The umbilicus is the centre of the target.

Hu *et al.* (1993) found a similar periodic orbit experimentally, with Prandtl number 0.93 and aspect ratio 41. They found that the centre of the target moves, followed by emission of radially travelling waves. Here a similar travelling wave has been predicted, although it is in perfectly axisymmetric convection. In their results, the oscillations stopped after a few cycles, whereas here they persist. Figure 12 shows pictures of the two periodic orbits for comparison, and as can be seen, they are qualitatively similar. The fact that the experimental oscillations stop may be because the periodic orbit found is in fact unstable to a non-axisymmetric perturbation. This will be investigated in a future paper.

All the phase portraits for this system can be drawn in two dimensions, see figure 8, which suggests the possibility of approximating the convection equations by a two-dimensional system whose behaviour is qualitatively the same. There is no way of deriving such a system analytically although ad hoc second-order equations can be written down. One possibility, from work by Riecke, Crawford & Knobloch (1988), is the system

$$\dot{z} = \mu z + \bar{z} + (-1 + \mathrm{i}a)|z|^2 z,$$

where $a \in \mathbb{R}$ and $\mu, z \in \mathbb{C}$. With $a = 0.8$ for example, this system can exhibit much

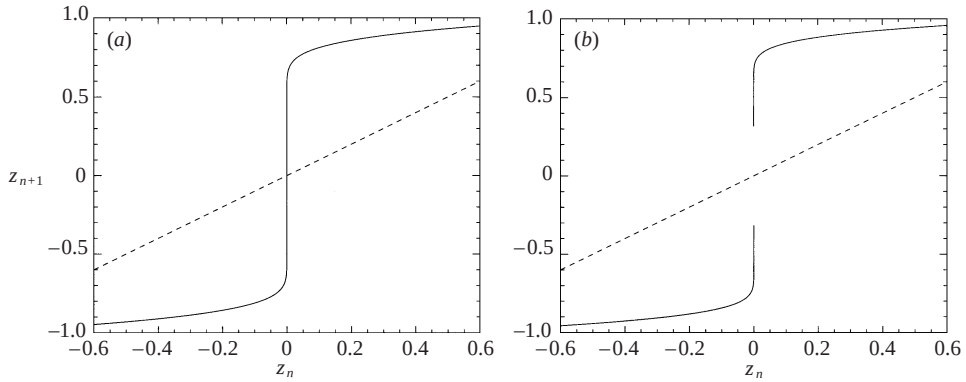

FIGURE 13. Graphs of z_{n+1} against z_n with $A = 1$, $\lambda_+ = 1$ $\mu = 0$. (*a*) $\delta = 0.01$, (*b*) $\delta = -0.01$. The dashed lines are graphs of $z_{n+1} = z_n$, so that the fixed points of the map are given by the intersections of the two graphs.

of the behaviour found here. Taking suitable cuts in the complex μ-plane, bifurcation diagrams that are qualitatively the same as figures 6(*a*), 6(*b*) and 6(*c*) can be produced. However, since the nonlinear behaviour cannot be derived analytically, this system will probably not provide much more insight. Harris, Bassom & Soward (2002) also found a qualitatively similar bifurcation structure in a model of spherical Couette flow. All these systems behave similarly because they all have the same symmetry properties.

The methods outlined can be extended to non-axisymmetric convection in a straightforward manner, which is work currently in progress. However, for the non-axisymmetric case the truncated system will contain many more equations, since the non-axisymmetric eigenfunctions must also be included. There is also no symmetry argument to exclude the toroidal eigenfunctions corresponding to that in § 2.2, and these eigenfunctions will appear immediately after onset. One phenomenon that may be studied using these techniques is meandering of a spiral tip or of the centre of the target (see Barkley, Kness & Tuckerman 1990). The tip of a spiral may stay stationary or it can move, either tracing out a circular path or performing epicycles (circles upon circles). At present it is not known for what parameter values the different types of meandering occur. The analysis described here could be used to help predict these regions and will be the subject of a future paper.

I wish to thank Michael Proctor and Alastair Rucklidge for many helpful conversations and guidance. The numerical bifurcations were computed with the help of AUTO (Doedel *et al.* 1997) and DsTool (Guckenheimer *et al.* 1991). I am grateful to the EPSRC for a research studentship and to Trinity College for travel support.

Appendix. Analysis of the behaviour where the curve of gluing bifurcations meets the curve of pitchfork bifurcations

The positions of the curves near this point may be calculated theoretically using a small-box procedure. The calculation is explained in detail here as it is not available in the literature, although a similar calculation was done by Hirschberg & Knobloch (1993) for a Šil'nikov–Hopf bifurcation point: the solution presented here can be found by letting the frequency of the travelling wave created at the Hopf bifurcation tend to zero. It is done in two dimensions since near this point there is an attracting

two-dimensional invariant manifold on which all the dynamics lie. The coordinates are denoted by x and y where the x-axis is in the direction of the local unstable manifold and the y-axis is in the direction of the local stable manifold. The phase space is split into two regions by placing a square box of side length $2h$, where h is small, centred on the origin (the conduction solution). Inside the box, the dynamics are approximated by the simplified system

$$\dot{x} = \lambda_+ x, \qquad \dot{y} = \lambda_- y - y^3,$$

where λ_+ is the positive eigenvalue at the origin and λ_- is the largest negative eigenvalue there. Usually $\dot{y} = \lambda_- y$, but here the extra term is needed since λ_- is near zero (it passes through zero at the pitchfork bifurcation). Outside the box, if a trajectory leaves the box at the point (h, y) then it is assumed to return to the box at $(-\mu + Ay, h)$ where μ is a small parameter and A is an order one constant. If the trajectory leaves the box at $(-h, y)$ then due to the symmetry κ it must return at $(\mu + Ay, -h)$. This system can be solved exactly, and using the lines $y = \pm h$ as Poincaré sections, if the trajectory starts from (x_0, y_0) where $y_0 = \pm h$ and returns for the nth time to one of the Poincaré sections at the point (x_n, y_n), then the recurrence relation

$$x_{n+1} = -\mathrm{sgn}(x_n)\mu + \mathrm{sgn}(y_n)A\sqrt{\frac{-\lambda_+\delta}{1 - |x_n/h|^{-2\delta}(1 + \lambda_+\delta/h^2)}}, \tag{A 1a}$$

$$y_{n+1} = \mathrm{sgn}(x_n)h, \tag{A 1b}$$

is obtained, where $\delta = -\lambda_-/\lambda_+$. By letting $z_n = x_n y_n$ (Lyubimov & Byelousova 1993), the system becomes one-dimensional,

$$z_{n+1} = -\mu h + \mathrm{sgn}(z_n)Ah\sqrt{\frac{-\lambda_+\delta}{1 - |z_n/h^2|^{-2\delta}(1 + \lambda_+\delta/h^2)}}. \tag{A 2}$$

A graph of z_{n+1} against z_n is shown for two different values of δ for the case $\mu = 0$ in figure 13. The qualitative features of the graph do not change as A or λ_+ are varied, and increasing μ simply translates the graph down by μh. Notice that the graphs are very similar except for their behaviour near $z_n = 0$. If $\delta > 0$ then the graph is continuous at zero whereas if $\delta < 0$ then the discontinuity is $2A\sqrt{-\lambda_-}$. Fixed points z_* of equation (A 2) represent periodic orbits in phase space, which are stable if the absolute value of the gradient of the solid curve is less than one and unstable otherwise. Note that $-h^2 \leqslant z_* \leqslant h^2$, so only fixed points near zero should be considered, and also that a fixed point z_* in equation (A 2) does not necessarily imply a fixed point for the corresponding values x_* and y_* of x and y. There are two different possibilities for the periodic orbit depending on the value of z_*.

(i) If $z_* > 0$ then (x_*, y_*) and $(-x_*, -y_*)$ are fixed points of the system (A 1), so there are two periodic orbits, which are reflections of each other in κ, as in figure 14(a).

(ii) If $z_* < 0$ then (x_*, y_*) is a period-two point of (A 1), and is mapped to $(-x_*, -y_*)$. In this case there is only one periodic orbit with symmetry $\tilde{\kappa}$, as shown in figure 14(b).

When $\delta > 0$ as in figure 13(a), if $\mu > 0$ then $z_* > 0$, meaning that there are two unstable periodic orbits, figure 8(l), whereas if $\mu < 0$ then $z_* < 0$ so there is one unstable symmetric periodic orbit as in figure 8(j), and a gluing bifurcation at $\mu = 0$, figure 8(k). When $\delta < 0$, for μ near zero there are no fixed points and so no periodic orbits near the saddle points, figure 8(g). As μ is increased above $A\sqrt{\lambda_+\delta}$, a fixed point $z_* > 0$ appears, so two unstable periodic orbits are created in a global bifurcation, figures 8(h) and 8(i), which is the homoclinic bifurcation described earlier. Similarly,

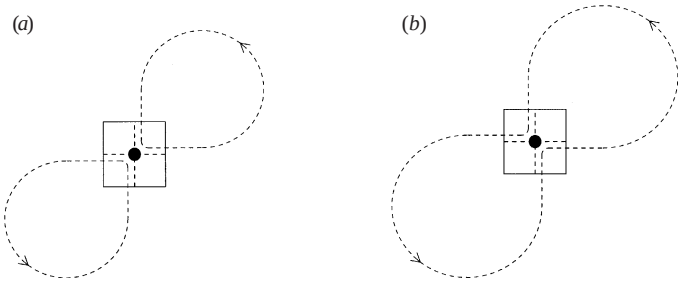

FIGURE 14. (*a*) The periodic orbit if $z_* > 0$, (*b*) the periodic orbit if $z_* < 0$.

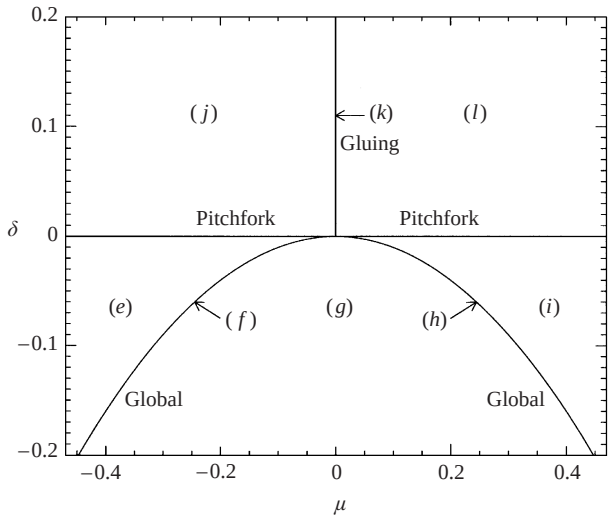

FIGURE 15. Diagram showing the bifurcation curves in the neighbourhood of the point $\delta = 0$, $\mu = 0$. The phase portraits in the different regions are shown in figure 8 and the labels also correspond to that figure.

as μ is decreased to below $-A\sqrt{\lambda_+\delta}$, the heteroclinic global bifurcation occurs creating an unstable periodic orbit, figures 8(*f*) and 8(*e*). The boundaries in (μ, δ) parameter space between the different regions are shown in figure 15. The layout of the curves of bifurcations agrees qualitatively with that shown in figure 9(*b*).

REFERENCES

BARKLEY, D., KNESS, M. & TUCKERMANN, L. S. 1990 Spiral-wave dynamics in a simple model of excitable media: the transition from simple to compound rotation. *Phys. Rev.* A **42**, 2489–2492.

BATCHELOR, G. K. & NITSCHE, J. M. 1993 Instability of stratified fluid in a vertical cylinder. *J. Fluid Mech.* **252**, 419–448.

BEHRINGER, R. P. & GAO, H. 1983 Time dependence in Rayleigh–Bénard convection with a variable cylindrical geometry. *Phys. Rev. Lett.* **50**, 1199–1202.

BERDAU, M., KARPOWICZ, A., YELENIN, G. G., CHRISTMANN, K. & BLOCK, J. H. 1997 Kinetic phase diagram for CO oxidations on Pt(210): pattern formation in the hysteresis and oscillation regions. *J. Chem. Phys.* **106**, 4291–4308.

CHARLSON, G. S. & SANI, R. L. 1970 Thermoconvective instability in a bounded cylindrical fluid layer. *Intl J. Heat Mass Transfer* **13**, 1479–1496.

CRAWFORD, J. D., GOLUBITSKY, M., GOMES, M. G. M., KNOBLOCH, E. & STEWART, I. N. 1991 Boundary conditions as symmetry constraints. In *Singularity Theory and its Applications, Warwick 1989,*

Part II (ed. M. Roberts & I. N. Stewart). Lecture Notes in Mathematics, vol. 1463, pp. 61–79. Springer.

Doedel, E. J., Champneys, A. R., Fairgrieve, T. F., Kuznetsov, Y. A., Sandstede, B. & Wang, X. 1997 AUTO. Available via ftp from ftp://ftp.cs.concordia.ca/pub/doedel/auto.

Edwards, W. S. & Fauve, S. 1994 Patterns and quasi-patterns in the Faraday experiment. *J. Fluid Mech.* **278**, 123–148.

Guckenheimer, J. & Holmes, P. 1986 *Nonlinear Oscillations, Dynamical Systems and Bifurcations of Vector Fluids*. Springer.

Guckenheimer, J., Myers, M. R., Wicklin, F. J. & Worfolk, P. A. 1991 DsTool. Available via ftp from ftp://macomb.cam.cornell.edu/pub/dstool.

Harris, D., Bassom, A. P. & Soward, A. M. 2002 Global bifurcation to travelling waves with application to spherical Couette flow *Physica* D (to appear).

Hirschberg, P. & Knobloch, E. 1993 Šil'nikov–Hopf bifurcation. *Physica* D **62**, 202–216.

Hu, Y., Ecke, R. & Ahlers, G. 1993 Convection near threshold for Prandtl numbers near 1. *Phys. Rev*. E **48**, 4399–4413.

Jones, C. A., Moore, D. R. & Weiss, N. O. 1976 Axisymmetric convection in a cylinder. *J. Fluid Mech.* **73**, 353–388.

Koschmieder, E. L. 1993 *Bénard Cells and Taylor Vortices*. Cambridge University Press.

Liang, S. F., Vidal, A. & Acrivos, A. 1969 Buoyancy-driven convection in cylindrical geometries. *J. Fluid Mech.* **36**, 239–256.

Lorenz, E. N. 1963 Deterministic non-periodic flow. *J. Atmos. Sci.* **20**, 130–141.

Lyubimov, D. V. & Byelousova, S. L. 1993 Onset of homoclinic chaos due to degeneracy in the spectrum of the saddle. *Physica* D **62**, 317–322.

Plapp, B. B., Egolf, D. A. & Bodenschatz, E. 1998 Dynamics and selection of giant spirals in Rayleigh–Bénard convection. *Phys. Rev. Lett*. **81**, 5334–5337.

Riecke, H., Crawford, J. D. & Knobloch, E. 1988 Time-modulated oscillatory convection. *Phys. Rev. Lett*. **61**, 1942–1945.

Rosenblat, S., Davis, S. H. & Homsy, G. M. 1982 Nonlinear Marangoni convection in bounded layers. Part 1. Circular cylindrical containers. *J. Fluid Mech.* **120**, 91–122.

Rüdiger, S. & Feudel, F. 2000 Pattern formation in Rayleigh–Bénard convection in a cylinder container. *Phys. Rev*. E **62**, 4927–4931.

Tuckerman, L. S. & Barkley, D. 1988 Global bifurcation to traveling waves in axisymmetric convection. *Phys. Rev. Lett*. **61**, 408–411.

Vidal, C., Pagola, A., Bodet, J. M., Hanusse, P. & Bastardie, E. 1986 Statistical experimental study of target patterns exhibited by the oscillating Belousov–Zhabotinsky reaction. *J. Phys. Paris* **47**, 1999–2009.

Weijer, C. J. 1999 Morphogenetic cell movement in dictyostelium. *Semin. Cell Dev. Biol.* **10**, 609–619.